Ancilla-assisted measurements on quantum ensembles: general protocols and applications in NMR quantum information processing

T. S. Mahesh[1,*], Abhishek Shukla[1], Swathi S. Hegde[1], C. S. Sudheer Kumar[1], Hemant Katiyar[1], Sharad Joshi[1] and K. R. Koteswara Rao[2]

[1]Department of Physics and NMR Research Centre, Indian Institute of Science Education and Research, Pune 411 008, India
[2]Department of Physics and Centre for Quantum Information and Quantum Computation, Indian Institute of Science, Bengaluru 560 012, India

Quantum ensembles form easily accessible architectures for studying various phenomena in quantum physics, quantum information science and spectroscopy. Here we review some recent protocols for measurements in quantum ensembles by utilizing ancillary systems. We also illustrate these protocols experimentally via nuclear magnetic resonance techniques. In particular, we shall review noninvasive measurements, extracting expectation values of various operators, characterizations of quantum states and quantum processes, and finally quantum noise engineering.

Keywords: Contextuality, expectation values, joint probabilities, noninvasive measurement, process tomography.

Introduction

UNLIKE the classical measurements, measurements in quantum physics affect the dynamics of the system. Moreover, often a particular experimental technique may offer only a limited set of observables which can be directly measured. The complete characterization of a quantum state or a quantum process requires, in general, a series of measurements of noncommuting observables – requiring repeated state preparation, and a large number of independent measurements. In this article, we review recent progresses in the measurement of quantum ensembles and explain how to overcome the above challenges. Here we exploit the presence of an *ancillary* register interacting with the *system* that is to be measured. In the following section we show how to realize noninvasive measurements using ancillary qubits. Extracting expectation values of various types of operators and related applications are described in the next section. We then describe an efficient protocol for complete quantum state characterization and quantum process tomography. We also narrate our experiments on noise engineering using ancillary qubits, and finally summarize all the topics. In all the sections, we illustrate the protocols experimentally using nuclear magnetic resonance (NMR) techniques.

Noninvasive measurements

A classical measurement can in principle be *noninvasive* in the sense it has no effect on the dynamics of the system. The same is not true in general for a quantum system, wherein the process of measurement itself may affect the dynamics of the system. However, as explained below, ancillary qubits can be utilized to realize certain quantum measurements without much disturbance, and hence extract probabilities or expectation values noninvasively to a great extent. Such measurements are often termed as *noninvasive quantum measurements*.

Consider the example of a single qubit initialized in state ρ (Figure 1 *a*) and a dichotomic observable Q with eigenvalues $q \in \{0, 1\}$. Suppose we need to extract the joint probabilities $P(q_1, q_2)$ at two time instances, one before applying an unitary U and the other after applying U (Figure 1 *a*). To realize the first measurement noninvasively, we utilize an *ancilla* qubit (Figure 1 *b*), a CNOT gate, and a final two-qubit projective measurement in $Q \otimes Q$ basis. The CNOT operation copies the probabilities of $P(q_1)$ onto the ancilla qubit without projecting the system state. Denoting the first qubit as the ancilla and

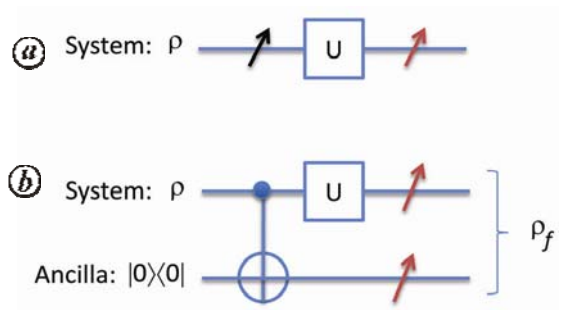

Figure 1. Circuits describing invasive and non-invasive measurements. The first measurement is invasive in (***a***). The same is replaced by a noninvasive measurement in (***b***). The final measurements are invasive in both.

*For correspondence. (e-mail: mahesh.ts@iiserpune.ac.in)

the second qubit as the system, the diagonal elements of the joint density operator ρ_f store the joint probabilities, i.e. $P(q_1, q_2) = \langle q_1 q_2 | \rho_f | q_1 q_2 \rangle$. The joint probabilities can thus be extracted by a final strong measurement or by a diagonal density matrix tomography[1]. Knee *et al.*[2] argued that since CNOT operator flips the ancilla qubit if the system qubit is in state $|1\rangle$, the circuit is not quite noninvasive. They also proposed a simple variation, in which $P(0, 0)$ and $P(0, 1)$ are measured using the CNOT operator, while $P(1, 0)$ and $P(1, 1)$ are measured using an anti-CNOT operator (which flips the ancilla only if the system qubit is in state $|1\rangle$). In this procedure, called *ideal negative-result measurement* (INRM), all the joint probabilities are measured without flipping the ancilla qubit, and therefore is considered *more noninvasive*. In the following we describe the application of INRM in studying the Leggett–Garg inequality (LGI).

LGI provides one way of distinguishing quantum behaviour from *macrorealism*. Macrorealism is based on the following assumptions: (i) the object remains in one or the other of many possible states at all times, and (ii) the measurements are noninvasive, i.e. they reveal the state of the object without disturbing the object or its future dynamics. LGI sets up macrorealistic bounds on linear combinations of two-time correlations of a dichotomic observable belonging to a single dynamical system[3]. Quantum systems are incompatible with these criteria and often violate bounds on correlations derived from them, thereby allowing us to distinguish the quantum behaviour from macrorealism. Violations of LGI by quantum systems have been investigated and demonstrated experimentally in various systems[1,4–13]. An entropic formulation of LGI has also been introduced by Usha Devi *et al.*[14] in terms of classical Shannon entropies associated with classical correlations. We had reported an experimental demonstration of violation of entropic LGI (ELGI) in an ensemble of spin-1/2 nuclei using NMR techniques[1]. The simplest ELGI study involves three sets of two-time joint measurements of a dynamic observable belonging to a 'system' qubit at time instants (t_1, t_2), (t_2, t_3) and (t_1, t_3). The first measurement in each case must be noninvasive, and can be performed with the help of an ancilla qubit.

Usha Devi *et al.*[17] have shown theoretically that for n-equidistant measurements on a spin-s system, the information deficit

$$D_n(\theta) = \frac{(n-1)H[\theta/(n-1)] - H[\theta]}{\log_2(2s+1)} \geq 0. \quad (1)$$

Here the conditional entropies $H(\theta)$ are obtained by the conditional probabilities

$$H\left(\frac{m\theta}{n-1}\right) = H(Q_n \mid Q_{n-m})$$

$$= -\sum_{q_{n-m}, q_n} P(q_n \mid q_{n-m}) \log_2 P(q_n \mid q_{n-m}),$$

where $m \in \{1, \ldots, n\}$. The conditional probabilities in turn are calculated from the joint probabilities using Bayes theorem

$$P(q_j \mid q_k) P(q_k) = P(q_j, q_k). \quad (2)$$

We studied ELGI experimentally by treating the ^{13}C and ^{1}H nuclear spins of $^{13}CHCl_3$ (dissolved in $CDCl_3$) as the system and the ancilla qubits respectively (Figure 2). The resonance offset of ^{13}C was set to 100 Hz and that of ^{1}H to 0 Hz (on resonant). The two spins have an indirect spin–spin coupling constant $J = 209.2$ Hz. The NMR experiments were carried out at an ambient temperature of 300 K on a 500 MHz Bruker NMR spectrometer.

As described in earlier, two sets of experiments were performed, one with CNOT and the other with anti-CNOT[1]. The joint entropies were calculated using the experimental probabilities and the information deficit (in bits) was calculated using the expression $D_3 = 2H(Q_2|Q_1) - H(Q_3|Q_1)$. The theoretical and experimental values of D_3 for various rotation angles θ are shown in Figure 2. According to quantum theory, a maximum violation of $D_3 = -0.134$ should occur at $\theta = \pi/4$. The corresponding experimental value, $D_3(\pi/4) = -0.114 \pm 0.027$, indicates a clear violation of ELGI.

Our other experiments involving noninvasive measurements include: (i) illustrating the inconsistency of quantum marginal probabilities with classical probability theory[1], and (ii) demonstrating that quantum joint probabilities cannot be obtained from moment distribution[15].

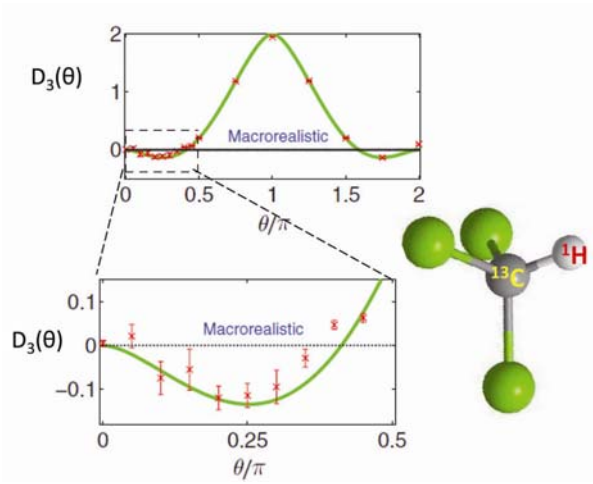

Figure 2. Information deficit D_3 versus θ obtained using INRM procedure. The mean experimental D_3 values are shown as symbols. The curves indicate theoretical D_3. The horizontal lines at $D_3 = 0$ indicate the lower bounds of the macrorealism territories (figure reproduced from Athalye *et al.*[1]).

Extracting expectation values

Often experimental set-ups allow direct detection of only a limited set of observables and to extract their expectation values. For example, in NMR only transverse magnetization operators ($\langle\sigma_x\rangle$ and $\langle\sigma_y\rangle$) are directly observable via real and imaginary components of induced emf. Figure 3 describes the circuits for measuring expectation values of different types of operators using an ancilla qubit. Here the expectation values $\langle\sigma_x\rangle$ and $\langle\sigma_y\rangle$ of ancilla qubit reveal the expectation values of different types of operators acting on system qubit. Applications of such circuits are illustrated with the help of following experiments: (a) estimation of Franck–Condon factors (FCFs), and (b) investigation of quantum contextuality (QC).

Estimation of Franck–Condon factors

The Franck–Condon principle states that the transition probability between two vibronic levels depends on the overlap between the respective vibrational wave functions[16]. FCFs dictate the intensities of vibronic transitions, and therefore their estimation is an important task in understanding absorption and fluorescence spectra and related phenomena such as photo-induced dissociations[17].

We modelled the electronic ground and excited vibrational levels as eigenstates of two harmonic potentials V_1 and V_2 respectively. To simulate the one-dimensional case, we choose the potentials $V_1 = x^2/2$ and $V_2 = (x-b)^2/2 + \Delta E$, which are identical up to an overall displacement b in position and/or in energy ΔE.

Thus the vibrational Hamiltonians for the two electronic states are

$$\mathcal{H}_1 = \mathbf{p}^2/2 + \mathbf{x}^2/2,$$

$$\mathcal{H}_2 = \mathbf{p}^2/2 + (\mathbf{x}-b)^2/2 + \Delta E. \tag{3}$$

The FCF between $|m\rangle$ of the electronic ground state and $|n\rangle$ of the electronic excited state is given by[16]

$$f_{m,n'}(b) = |\langle m|n'\rangle|^2 = \left|\int_{-\infty}^{\infty} \psi_m^*(x)\psi_{n'}(x,b)\,\mathrm{d}x\right|^2, \tag{4}$$

where $\psi_m(x)$, $\psi_{n'}(x, b)$ are the corresponding position wave functions.

Estimation of FCF, $f_{m,n'}$, is equivalent to measurement of expectation value of the projection $P_m = |m\rangle\langle m|$ after preparing the system in excited state $|n'\rangle$ since[18]

$$f_{m,n'} = \langle n'|m\rangle\langle m|n'\rangle = \langle P_m\rangle_{n'}. \tag{5}$$

Three spin-1/2 ^{19}F nuclei of iodotriuoroethylene (C_2F_3I) dissolved in acetone-D_6 form a three-qubit NMR quantum simulator (Figure 4). F_1 qubit is chosen to be the

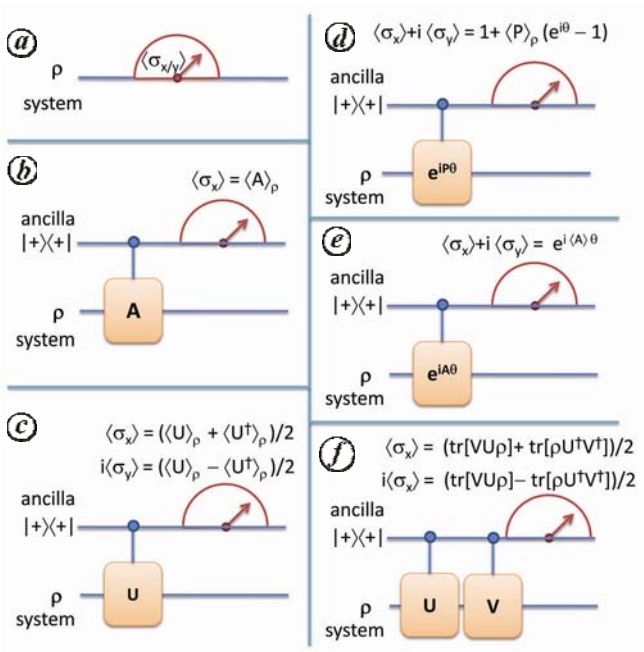

Figure 3. Circuits for (***a***) NMR measurements of $\langle\sigma_x\rangle$ and $\langle\sigma_y\rangle$, (***b***) standard Moussa protocol for expectation values of Hermitian-unitary operator A[6]. Circuits for measuring expectation values of (***c***) a unitary operator U[18], (***d***) a projector P[18], (***e***) a diagonal Hermitian operator A and (***f***) joint expectation values of noncommuting unitaries U and V[15].

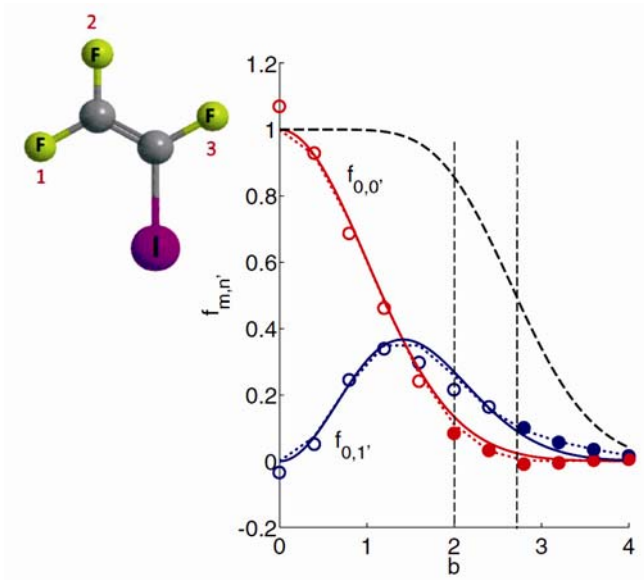

Figure 4. Experimental Franck–Condon factors (FCFs) (circles) corresponding to four-level harmonic oscillators versus the displacement b (in atomic units). The simulated FCFs (dotted lines) for the four-level system and analytical FCFs (smooth lines) for infinite-level system are also shown for comparison. The dashed curve at the top corresponds to the normalization used. The thin vertical dashed lines at $b = 2$, $1 + \sqrt{3}$ mark the beginning of classically forbidden regions for $f_{0,0'}$, $f_{0,1'}$ respectively. (Inset) Molecular structure and qubit labelling are shown (Figure reproduced from Joshi *et al.*[18]).

ancilla and the other two qubits are chosen representing the lowest four levels of the Harmonic oscillator[18]. The vibrational levels of the electronic ground state are encoded onto the spin states such that $|0\rangle = |\uparrow\uparrow\rangle$, $|1\rangle = |\uparrow\downarrow\rangle$, $|2\rangle = |\downarrow\uparrow\rangle$ and $|3\rangle = |\downarrow\downarrow\rangle$. The preparation of excited state $|n'\rangle$ can be achieved by first initializing the system in the corresponding state $|n\rangle$ of the electronic ground state and translating it in position from origin ($x = 0$) to the point $x = b$. This translation can be achieved by the unitary operator

$$U_T(b) = e^{-ipb}. \tag{6}$$

Finally the expectation values $\langle P_m\rangle$ were measured experimentally using the circuit shown in Figure 3 *d*, and then the FCFs $f_{m,n}$ were obtained[18] using eq. (5). The results described in Figure 4 display a good correspondence with the theoretically expected values, indicating the success of the experimental protocols.

Investigation of QC in a harmonic oscillator

QC states that the outcome of the measurement depends not only on the system and the observable but also on the context of the measurement, i.e., on other compatible observables which are measured along with[19]. Consider the following non-local hidden variable (NCHV) inequality[20]

$$\begin{aligned}\mathbf{I} &= \langle AB + BC + CD - AD\rangle \\ &= \langle AB\rangle + \langle BC\rangle + \langle CD\rangle - \langle AD\rangle \le 2.\end{aligned} \tag{7}$$

Su *et al.*[21] theoretically studied QC of eigenstates of 1D-QHO. They introduced two sets of pseudospin operators

$$\begin{aligned}&\Gamma_x = \sigma_x \otimes \mathbb{1},\ \Gamma_y = \sigma_z \otimes \sigma_y,\ \Gamma_z = -\sigma_y \otimes \sigma_y, \\ &\Gamma'_x = \sigma_x \otimes \sigma_z,\ \Gamma'_y = \mathbb{1} \otimes \sigma_y,\ \Gamma'_z = -\sigma_x \otimes \sigma_x,\end{aligned} \tag{8}$$

where $\mathbb{1}$ is a 2×2 identity matrix. Using these operators they defined the observables

$$\begin{aligned}&A = \Gamma_x,\ B = c_\beta\,\Gamma'_x + s_\beta \Gamma'_z = \sigma_x \otimes (c_\beta \sigma_z - s_\beta \sigma_x), \\ &C = \Gamma_z, D = c_\eta \Gamma'_x + s_\eta \Gamma'_z = \sigma_x \otimes (c_\eta \sigma_z - s_\eta \sigma_x),\end{aligned} \tag{9}$$

where $c_\beta = \cos\beta$, $s_\beta = \sin\beta$, $c_\eta = \cos\eta$ and $s_\eta = \sin\eta$. Here operators A, B, C, D are unitary and Hermitian, and accordingly have eigenvalues ± 1, with (A, B), (B, C), (C, D) and (D, A) forming compatible pairs. Su *et al.*[53] have shown that

$$\mathbf{I}^{\mathrm{QM}}_{|l\rangle\,\mathrm{QHO}} = 2\sqrt{2} > 2, \quad \text{if } (\beta,\eta)_l = \begin{cases}(-\pi/4, -3\pi/4)_0 \\ (3\pi/4, \pi/4)_1 \\ (\pi/4, 3\pi/4)_2 \\ (-3\pi/4, -\pi/4)_3\end{cases}, \tag{10}$$

where $\mathbf{I}^{\mathrm{QM}}_{|l\rangle\,\mathrm{QHO}}$ is the expression on the LHS of inequality in eq. (7), $l = 0$, 1, 2 and 3, and $|0\rangle_{\mathrm{QHO}}$, $|1\rangle_{\mathrm{QHO}}$, $|2\rangle_{\mathrm{QHO}}$ and $|3\rangle_{\mathrm{QHO}}$ are the first four energy eigenstates of 1D-QHO.

We encoded the first four energy eigenstates of 1D-QHO onto the four Zeeman eigenstates of a pair of spin-1/2 nuclei. The circuit shown in Figure 3 *f* was used to extract the expectation value of observables (*AB*, *BC*, *CD* and *DA*) in a joint measurement. We used three ^{19}F nuclear spins of trifluoroiodoethylene dissolved in acetone-D6 (inset, Figure 4) as the three-qubit register. The first spin, F_1, was used as an ancilla qubit and other spins, F_2 and F_3, as the system qubits. The results are shown in Figure 5. The maximum theoretical violation[22] is $2\sqrt{2} = 2.82$. The experimental value of maximum violation for $\mathbf{I}_0$, $\mathbf{I}_1$, $\mathbf{I}_2$ and $\mathbf{I}_3$ are 2.40 ± 0.017, 2.45 ± 0.025, 2.39 ± 0.016 and 2.42 ± 0.026 respectively[22]. There is a clear violation of the classical bound. Reduced violation than the theoretical value is due to T_2 decay and inhomogeneity in radio frequency (RF) pulses.

Ancilla-assisted quantum state tomography

In experimental quantum information studies, quantum state tomography (QST) is an important tool that is routinely used to characterize an instantaneous quantum state[20]. QST can be performed by a series of measurements of noncommuting observables which together enables one to reconstruct the complete complex density matrix[20]. In the standard method, the required number of independent experiments grows exponentially with the number of input qubits[23,24]. Anil Kumar and co-workers have illustrated QST using a single two-dimensional

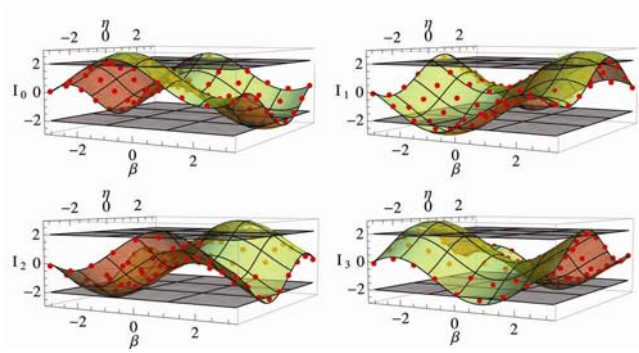

Figure 5. $\mathbf{I}_0$, $\mathbf{I}_1$, $\mathbf{I}_2$, and $\mathbf{I}_3$ represent evaluation of inequality in eq. (7) for eigenstates $|0\rangle_{\mathrm{QHO}}$, $|1\rangle_{\mathrm{QHO}}$, $|2\rangle_{\mathrm{QHO}}$ and $|3\rangle_{\mathrm{QHO}}$ respectively[22]. The curved surface represents theoretical values, and the points are experimental values. Flat planes at $I = 2$ and $I = -2$ represent classical bounds.

NMR spectrum[25]. Later Nieuwenhuizen and co-workers showed how to reduce the number of independent experiments in the presence of an ancilla register[26]. We refer to this method as ancilla-assisted QST (AAQST) and experimentally demonstrated it using NMR systems[27,28]. AAQST also allows single-shot mapping of density matrix which not only reduces the experimental time, but also alleviates the need to prepare the target state repeatedly[28].

To see how AAQST works, consider an input register of n-qubits associated with an ancilla register consisting of $\hat{n}$ qubits. The dimension of the combined system of $\tilde{n} = n + \hat{n}$ qubits is $\hat{N} = N\hat{N}$, where $\hat{N} = 2^{\hat{n}}$. A completely resolved NMR spectrum yields $\tilde{n}\tilde{N}$ real parameters. We assume that the ancilla register begins with the maximally mixed initial state, with no contribution to the spectral lines from it. The deviation density matrix of the combined system is $\tilde{\rho} = \rho \otimes 1/\hat{N}$. To perform AAQST, we apply a non-local unitary of the form

$$\tilde{U}_k = V \sum_{a=0}^{\hat{N}-1} U_{ka} \otimes |a\rangle\langle a|. \tag{11}$$

Here U_{ka} is the kth unitary on the input register dependent on the ancilla state $|a\rangle$ and V is the local unitary on the ancilla. The combined state evolves to

$$\tilde{\rho}^{(k)} = \tilde{U}_k \tilde{\rho} \tilde{U}_k^{\dagger}$$
$$= \frac{1}{\hat{N}} \sum_{m,m',a} \rho_{mm'} U_{ka} |m\rangle\langle m'| U_{ka}^{\dagger} \otimes V |a\rangle\langle a| V^{\dagger}. \tag{12}$$

Intensity of NMR spectrum is proportional to the observable

$$\sum_{j=1}^{\tilde{n}} \sigma_{jx} + \mathrm{i}\sigma_{jy}.$$

The spectrum of the combined system yields $\tilde{n}\tilde{N}$ linear equations. The minimum number of independent experiments needed is now $O(N^2/(\tilde{n}\tilde{N}))$. Choosing $\tilde{N} \gg N$, AAQST needs fewer than $O(N/n)$ experiments required in the standard QST. In particular, when $\tilde{n}\tilde{N} \geq N^2$, a single optimized unitary suffices for QST. Figure 6 illustrates the minimum number (K) of experiments required for various sizes of input and ancilla registers. As illustrated, QST can be achieved with only one experiment, if an ancilla of sufficient size is provided along with[28].

To demonstrate this procedure experimentally, we used three ^{19}F nuclei and two ^{1}H nuclei of 1-bromo-2,4,5-trifluorobenzene (BTFBz) partially oriented in a liquid crystal namely N-(4-methoxybenzaldehyde)-4-butylaniline (MBBA; Figure 7)[28]. We chose the three ^{19}F nuclei forming the input register and two ^{1}H nuclei forming the ancilla register.

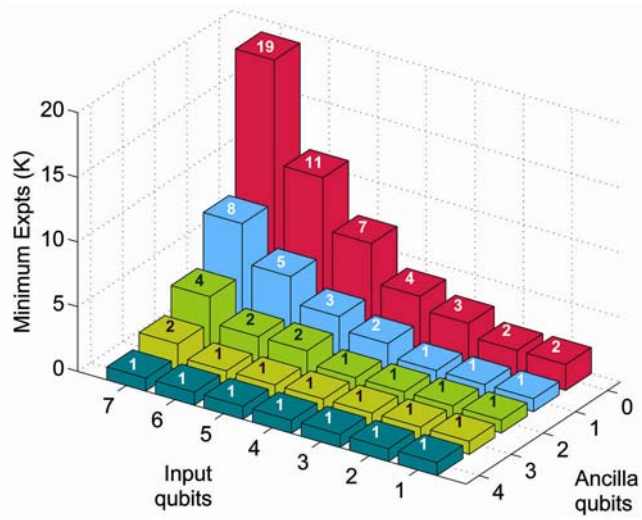

Figure 6. Minimum number of independent experiments required for quantum state tomography (QST) (with zero ancilla) and ancilla-assisted QST (AAQST) (figure reproduced from Shukla *et al.*[28]).

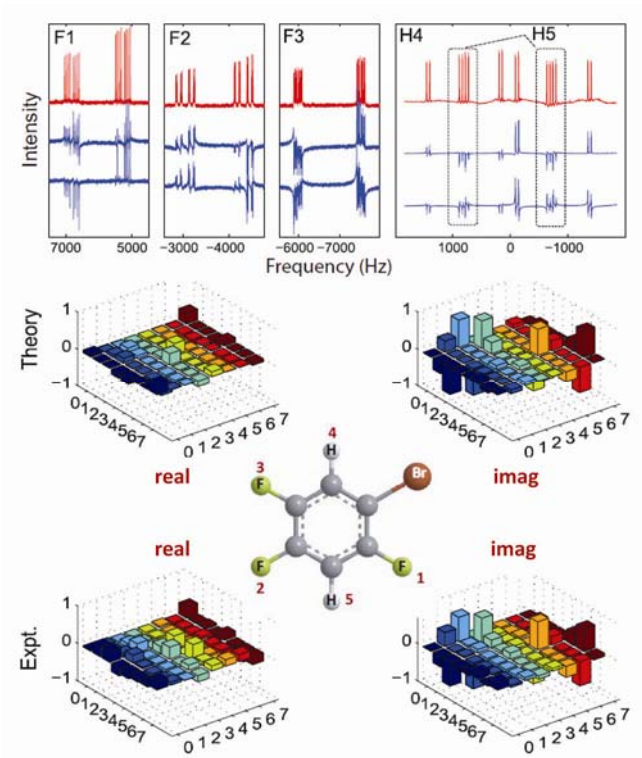

Figure 7. AAQST results for the state described in the text[28]. The reference spectrum is in the top trace. The real (middle trace) and the imaginary spectra (bottom trace) are obtained in a single-shot AAQST experiment. The bar plots correspond to theoretically expected density matrices (top row) and those obtained from AAQST experiments (bottom row). The molecular structure and the labelling scheme of 1-bromo-2,4,5-trifluorobenzene (BTFBz) is shown in the centre (figure reproduced from Shukla *et al.*[28]).

Figure 7 shows the experimental results corresponding to a particular density matrix obtained by applying unitary

$$U_0 = \left(\frac{\pi}{2}\right)_x^F \tau_0 (\pi)_x^H \tau_0 \left(\frac{\pi}{2}\right)_y^{F_1},$$

with $\tau_0 = 2.5$ ms, on thermal equilibrium state. The real and imaginary parts of the reconstructed density matrix along with the theoretically expected matrices are shown below the spectra in Figure 7. Fidelity of the experimental state with the theoretical state was 0.95. The entire three-qubit density matrix with 63 unknowns was estimated by a single NMR experiment[28].

Single-scan process tomography

Often one needs to characterize the overall process acting on a quantum system. Such a characterization, achieved by a procedure called quantum process tomography (QPT), is crucial in designing fault-tolerant quantum processors[29,30]. QPT is realized by considering the quantum process as a map from a complete set of initial states to final states, and experimentally characterizing each of the final states using QST[23]. Since QST by itself involves repeated preparations of a target state, QPT in general requires a number of independent experiments. Therefore, the total number of independent measurements required for QPT increases exponentially with the size of the system undergoing the process.

The physical realization of QPT has been demonstrated on various experimental set-ups[31–45]. Several developments in the methodology of QPT have also been reported[46,47]. In particular, it has been shown that ancilla-assisted process tomography (AAPT) can characterize a process with a single QST[31,36,48,49]. By combining AAQST and AAPT, we have shown that the entire QPT can be carried out with a single ensemble measurement[50]. We refer to this procedure as 'single-scan quantum process tomography (SSPT)'[50].

In the normal QPT procedure, the outcome of the process ε is expanded in a complete basis of linearly independent elements $\{\rho_1, \rho_2, \ldots, \rho_{N^2}\}$ as well as using operator-sum representation, i.e.

$$\varepsilon(\rho_j) = \sum_k \lambda_{jk} \rho_k = \sum_i E_i \rho E_i^\dagger. \tag{13}$$

The complex coefficients λ_{jk} can be extracted using QST. We can utilize a fixed set of basis operators $\{\tilde{E}_m\}$, and express $E_i = \sum_m e_{im} \tilde{E}_m$ so that

$$\varepsilon(\rho) = \sum_{mn} \tilde{E}_m \rho \tilde{E}_n^\dagger \chi_{mn}, \tag{14}$$

where $\chi_{mn} = \sum_i e_{im} e_{in}^*$. The χ matrix completely characterizes the process ε. Since the set $\{\rho_k\}$ forms a complete basis, it is also possible to express

$$\tilde{E}_m \rho_j \tilde{E}_n^\dagger = \sum_k \beta_{jk}^{mn} \rho_k, \tag{15}$$

where β_{jk}^{mn} can be calculated theoretically. Using eqs (13)–(15) and using the linear independence of $\{\rho_k\}$, we obtain

$$\beta\chi = \lambda, \tag{16}$$

from which χ matrix can be extracted by standard methods in linear algebra.

A comparison of QPT, AAPT and SSPT procedures for a single qubit process is presented in Figure 8 (ref. 50).

Estimates of the number of measurements for a small number of qubits shown in the first column of Table 1 illustrate the exponential increase of M_{QPT} with n.

The experimental demonstration of a single-qubit SSPT was carried out using iodotrifluoroethylene

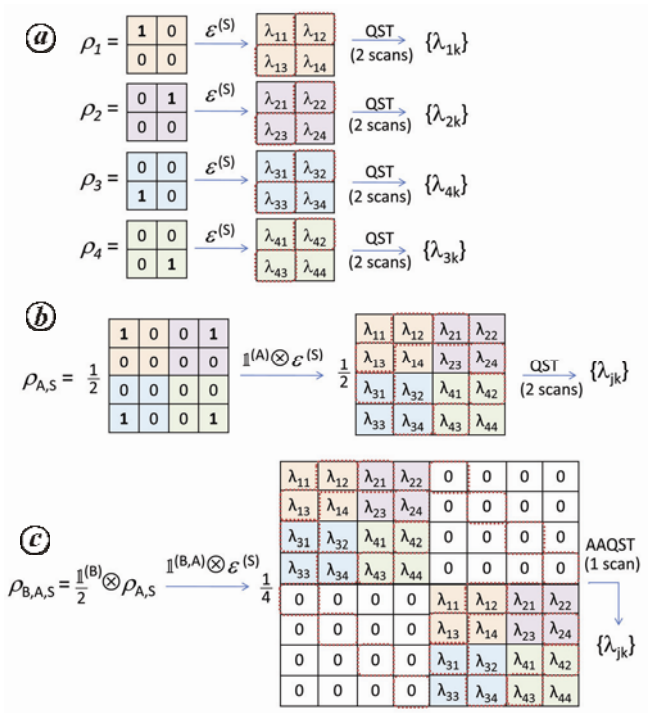

Figure 8. Illustrating (***a***) single-qubit quantum process tomography (QPT) requiring a total of eight NMR scans, (***b***) ancilla assisted process tomography (AAPT) requiring two NMR scans, and (***c***) single-scan quantum process tomography (SSPT) requiring a single-scan NMR experiment[50]. In each case, dotted lines are used to indicate the single-quantum elements of the density matrix which are directly observable. Other elements are observed by converting them to observable single-quantum coherences by using certain unitary operations in a subsequent scan(s) (figure reproduced from Shukla *et al.*[50]).

dissolved in acetone-D_6 as a three-qubit system (Figure 9)[50]. The experimentally obtained χ matrices for certain quantum processes using the single-scan procedure are shown in Figure 9.

Ancilla-assisted noise engineering

Preserving coherence is an important aspect to realize quantum processors, and hence various techniques have been developed to suppress decoherence. They include dynamical decoupling (DD) techniques[51–54], quantum error correction[55], adiabatic quantum computation[56], and use of decoherence-free subspaces[57]. Earlier Teklemariam *et al*. introduced artificial decoherence by achieving irreversible phase damping via constant perturbation of the environment qubits (by random classical fields), thus mimicking a large dimensional environmental bath. Such experiments provide insights about decoherence processes and may pave the way for improving decoherence suppression techniques.

Table 1. Comparison of number of scans and number of ancilla qubits (in parenthesis) required for n-qubit QPT, AAPT and SSPT

n	M_{QPT}	M_{AAPT}	(n_A)	M_{SSPT}	(n_A, n_B)
1	8	2	(1)	1	(1, 1)
2	32	4	(2)	1	(2, 2)
3	192	11	(3)	1	(3, 3)
4	1024	32	(4)	1	(4, 5)
5	7168	103	(5)	1	(5, 6)

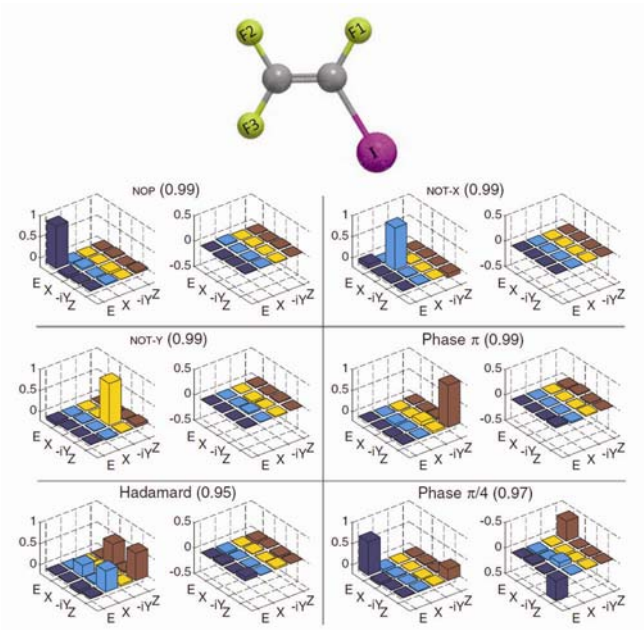

Figure 9. The barplots showing experimental χ-matrices for various quantum processes obtained using SSPT. In each case, the left and right barplots correspond to the real and imaginary parts respectively, and the fidelities are indicated in parenthesis (figure reproduced from Shukla *et al.*[50]).

In our work we simulated such a decoherence process on a NMR simulator with two qubits, where one acts as the system and the other as environment[58]. We then subjected the system qubit to certain DD sequences and observed their competition with the engineered decoherence through noise spectroscopy.

The two-qubit register was initially in the product state, $\rho(0) = \rho^s(0) \otimes \rho^e(0)$. Here $\rho^s(0)$ is the system state and $\rho^e(0)$ is the environment state. We chose ^{1}H and ^{13}C nuclear spins in ^{13}C-labelled chloroform ($^{13}CHCl_3$ dissolved in $CDCl_3$) as the system and environment qubits respectively. The NMR Hamiltonian is

$$\mathcal{H} = \pi\left(\nu_s\sigma_z^s + \nu_e\sigma_z^e + \frac{J}{2}\sigma_z^s\sigma_z^e\right), \tag{17}$$

where ν_s and ν_e are the resonant frequencies of the system and the environment qubits respectively, J the coupling strength between the two, and σ_z^s, σ_z^e are the Pauli operators. In a total duration T, the propagator $U = e^{-i\mathcal{H}T}$ entangles the system qubit with the environment qubit via the interaction J. We engineered decoherence by a series of RF kicks of arbitrary angles $\varepsilon \in [-\theta, \theta]$ on the environment qubit. These kicks induced arti-ficial decoherence on the system qubit. Teklemariam *et al.*[17] proved that induced decoherence of the system qubit depends on the kick-rate Γ, range of kick-angles θ, and coupling strength J[59]. Their model predicted that for small kick-angles ε and for lower kick rates Γ, decoherence rate $1/T_2$ increases linearly with Γ. After a certain value of Γ, $1/T_2$ saturates, and then it decreases exponentially with Γ.

Our experimental results for $\varepsilon \in [0°, 1°]$ and Γ = 25 kicks/ms are shown in Figure 10 (indicated by stars). For comparison we have also shown the decay of magnetization without kicks (indicated by filled circles).

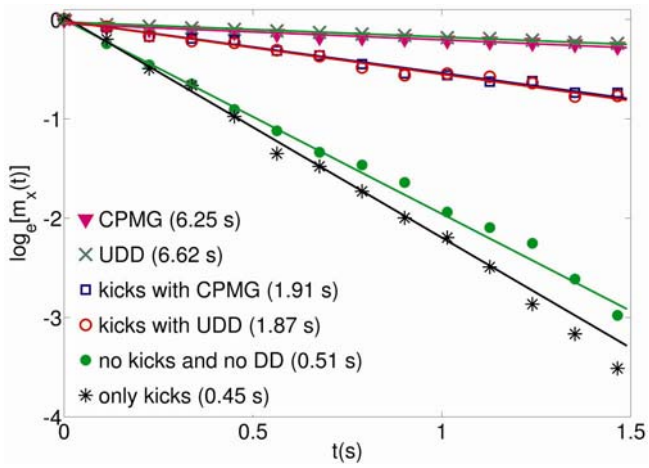

Figure 10. Logarithm of transverse magnetization $\log(M_x)$ as a function of time under different pulse sequences as indicated in the legend. Here τ = 3.2 ms, Γ = 25 kicks/ms, and $\varepsilon \in [0°, 1°]$. The T_2 values for various pulse sequences are shown in the legend (figure reproduced from Hegde and Mahesh[58]).

Evidently, the kicks on the environment have introduced additional decoherence thereby increasing the decay of system-coherence[58].

Dynamical decoupling attempts to inhibit decoherence of the system by rapid modulation of the system state so as to cancel the system–environment joint evolutions. The two standard DD sequences are: (i) CPMG[51] and (ii) UDD[52]. CPMG consists of a series of equidistant π pulses applied in the system qubits. In an N-pulse UDD of cycle time t_c, the time instant t_j of the jth π-pulse is given by

$$t_j = t_c \sin^2\left[\frac{\pi j}{2(N+1)}\right].$$

The results of the experiments for t_c = 22.4 ms and with different kick-parameters are shown in Figure 10. The competition between kicks-induced decoherence and DD sequences can be readily observed[58].

Noise spectroscopy provides information about noise spectral density, which is the frequency distribution of noise and is helpful in not only understanding the performance of standard DD sequences, but also in optimizing them[60–62]. In the limit of a large number of π pulses, the CPMG filter function resembles a delta peak at ω, and samples this particular spectral frequency. The amplitude of the noise $S(\omega)$ can be determined using the relation[63]

$$S(\omega) \simeq \frac{\pi^2}{4T_2(\omega)}.$$

Thus by measuring $T_2(\omega)$ for a range of $\omega = \pi/\tau$ values, we can scan the profile of $S(\omega)$.

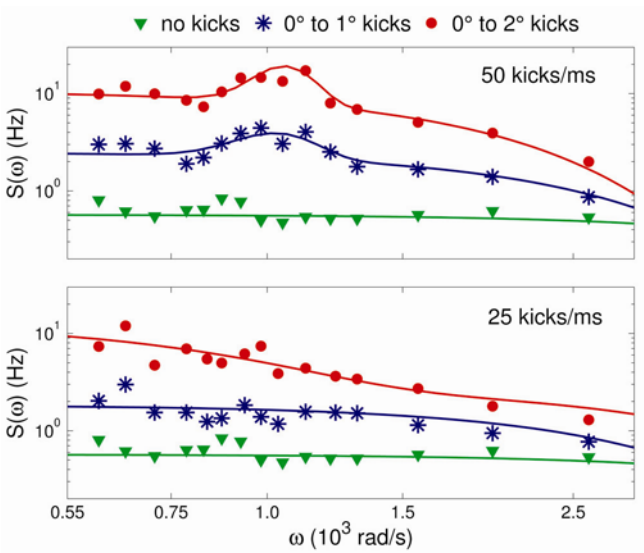

Figure 11. Experimental spectral density profiles with different kick-angles (as indicated in the legend) and with kick-rates of 50 kicks/ms (top trace) and 25 kicks/ms (bottom trace). In both the traces, experimental spectral density profile without kicks is also shown for comparison. The smooth lines correspond to fits with one or two Gaussians (figure reproduced from Hegde and Mahesh[58]).

The experimental spectral density profiles of only natural decoherence (lowest curve in each sub-plot), and with kicks of different kick-parameters are shown in Figure 11 (ref. 24). Clearly, the effect of kicks is to increase the area under the spectral density profiles and thereby leading to faster decoherence. Moreover, for a given kick-rate Γ, larger the range of kick-angles, higher is the spectral density-profile[58].

Summary

In this article, we have described several recent protocols for efficient measurements on quantum systems, and illustrated their NMR implementations.

We have described ancilla-assisted noninvasive measurements, where the measurement result of an intermediate observable was temporarily stored in an ancilla qubit. A final joint-measurement of the system–ancilla register revealed the joint probabilities in a noninvasive way. We also showed the application of this technique in studying entropic LGI[1].

Then, we described extracting expectation values of various types of operators. Applications of these methods are illustrated in the estimation of Franck–Condon coefficients and in the investigation of quantum contextuality[18,22].

We have also described efficient ways to characterize quantum states and quantum processes by exploiting ancilla qubits. We have illustrated single-scan quantum state tomography as well as single-scan quantum process tomography using NMR systems. These techniques not only alleviate the need of repeated measurements, but also allow the study of random states or dynamic processes[28,50].

Finally we have described ancilla-assisted noise engineering, where random fields applied to the ancilla qubits cause controllable decoherence on the system qubits. We have illustrated this phenomena using a two-qubit NMR system, and studied the engineered decoherence by measuring noise spectrum[58].

Although we have used NMR techniques to demonstrate the above protocols experimentally, these procedures are quite general in nature, and can be easily adopted to other experimental techniques as well.

1. Athalye, V., Roy, S. S. and Mahesh, T. S., Investigation of the Leggett–Garg inequality for precessing nuclear spins. *Phys. Rev. Lett.*, 2011, **107**(13), 130402-1 to 5.
2. Knee, G. C., Gauger, E. M., Briggs, G. A. D. and Benjamin, S. C., Comment on A scattering quantum circuit for measuring Bell's time inequality: a nuclear magnetic resonance demonstration using maximally mixed states. *New J. Phys.*, 2012, **14**(5), 058001-1 to 6.
3. Leggett, A. J. and Garg, A., Quantum mechanics versus macroscopic realism: is the flux there when nobody looks? *Phys. Rev. Lett.*, 1985, **54**(9), 857–860.

4. Dressel, J., Broadbent, C. J., Howell, J. C. and Jordan, A. N., Experimental violation of two-party Leggett–Garg inequalities with semiweak measurements. *Phys. Rev. Lett*., 2011, 106(4), 040402-1 to 4.
5. Emary, C., Leggett–Garg inequalities for the statistics of electron transport. *Phys. Rev. B*, 2012, **86**(8), 085418-1 to 5.
6. Goggin, M., Almeida, M., Barbieri, M., Lanyon, B., O'Brien, J., White, A. and Pryde, G., Violation of the Leggett–Garg inequality with weak measurements of photons. *Proc. Nat. Acad. Sci. USA*, 2011, **108**(4), 1256–1261.
7. Knee, G. C. *et al.*, Violation of a Leggett–Garg inequality with ideal non-invasive measurements. *Nature Commun.*, 2012, **3**, 606-1 to 6.
8. Lambert, N., Johansson, R. and Nori, F., Macrorealism inequality for optoelectromechanical systems. *Phys. Rev. B*, 2011, **84**(24), 245421-1 to 7.
9. Palacios-Laloy, A., Mallet, F., Nguyen, F., Bertet, P., Vion, D., Esteve, D. and Korotkov, A. N., Experimental violation of a Bell's inequality in time with weak measurement. *Nature Phys*., 2010, **6**(6), 442–447.
10. Souza, A. M., Oliveira, I. S. and Sarthour, R. S., A scattering quantum circuit for measuring Bell's time inequality: A nuclear magnetic resonance demonstration using maximally mixed states. *New J. Phys*., 2011, **13**(5), 053023-1 to 7.
11. Suzuki, Y., Iinuma, M. and Hofmann, H. F., Violation of Leggett–Garg inequalities in quantum measurements with variable resolution and back-action. *New J. Phys*., 2012, **14**(10), 103022-1 to 16.
12. Yong-Nan, S., Yang, Z., Rong-Chun, G., Jian-Shun, T. and Chuan-Feng, L., Violation of Leggett–Garg inequalities in single quantum dots. *Chin. Phys. Lett*., 2012, **29**(12), 120302-1 to 4.
13. Zhou, Z.-Q., Huelga, S. F., Li, C.-F. and Guo, G.-C., Experimental detection of quantum coherent evolution through the violation of Leggett–Garg inequalities. arXiv:1209.2176[quant-ph].
14. Usha Devi, A. R., Karthik, H. S., Sudha and Rajagopal, A. K., Macrorealism from entropic Leggett–Garg inequalities. *Phys. Rev. A*, 2013, **87**(5), 052103-1 to 5.
15. Karthik, H. S., Katiyar, H., Shukla, A., Mahesh, T. S., Usha Devi, A. R. and Rajagopal, A. K., Inversion of moments to retrieve joint probabilities in quantum sequential measurements. *Phys. Rev. A*, 2013, **87**(5), 052118-1 to 6.
16. Demtröder, W., *Atoms, Molecules and Photons*, Springer, 2010.
17. Bowers, W. D., Delbert, S. S., Hunter, R. L. and McIver Jr, R. T., Fragmentation of oligopeptide ions using ultraviolet laser radiation and Fourier transform mass spectrometry. *J. Am. Chem. Soc*., 1984, **106**(23), 7288–7289.
18. Joshi, S., Shukla, A., Katiyar, H., Hazra, A. and Mahesh, T. S., Estimating Franck–Condon factors using an NMR quantum processor. *Phys. Rev. A*, 2014, **90**(2), 022303-1 to 6.
19. Peres, A., Incompatible results of quantum measurements. *Phys. Lett. A*, 1990, **151**(34), 107–108.
20. Nielsen, M. A. and Chuang, I. L., *Quantum Computation and Quantum Information*, Cambridge University Press, New Delhi, 2010.
21. Su, H.-Y., Chen, J.-L., Wu, C., Yu, S. and Oh, C. H., Quantum contextuality in a one-dimensional quantum harmonic oscillator. *Phys. Rev. A*, 2012, **85**(5), 052126-1 to 5.
22. Katiyar, H., Sudheer Kumar, C. S. and Mahesh, T. S., Investigation of quantum contextuality in a harmonic oscillator using an NMR quantum simulator. arXiv:1503.05883[quant-ph].
23. Chuang, I. L., Gershenfeld, N., Kubinec, M. G. and Leung, D. W., Bulk quantum computation with nuclear magnetic resonance: Theory and experiment. *Proc. R. Soc. London Ser. A*, 1998, **454**(1969), 447–467.
24. Leung, D., Vandersypen, L., Zhou, X., Sherwood, M., Yannoni, C., Kubinec, M. and Chuang, I., Experimental realization of a two-bit phase damping quantum code. *Phys. Rev. A*, 1999, **60**(3), 1924–1943.
25. Das, R., Mahesh, T. S. and Kumar, A., Efficient quantumstate tomography for quantum-information processing using a two-dimensional Fourier-transform technique. *Phys. Rev. A*, 2003, **67**(6), 062304-1 to 6.
26. Allahverdyan, A. E., Balian, R. and Nieuwenhuizen, T. M., Determining a quantum state by means of a single apparatus. *Phys. Rev. Lett.*, 2004, **92**(12), 120402-1 to 4.
27. Peng, X., Du, J. and Suter, D., Measuring complete quantum states with a single observable. *Phys. Rev. A*, 2007, **76**(4), 042117-1 to 12.
28. Shukla, A., Rao, K. R. K. and Mahesh, T. S., Ancilla-assisted quantum state tomography in multiqubit registers. *Phys. Rev. A*, 2013, **87**(6), 062317-1 to 8.
29. Chuang, I. L. and Nielsen, M. A., Prescription for experimental determination of the dynamics of a quantum black box. *J. Mod. Opt.*, 1997, **44**(11–12), 2455–2467.
30. Poyatos, J. F., Cirac, J. I. and Zoller, P., Complete characterization of a quantum process: the two-bit quantum gate. *Phys. Rev. Lett*., 1997, **78**(2), 390–393.
31. Altepeter, J. B. *et al.*, Ancilla-assisted quantum process tomography. *Phys. Rev. Lett*., 2003, **90**(19), 193601-1 to 4.
32. Bialczak, R. C. *et al.*, Quantum process tomography of a universal entangling gate implemented with Josephson phase qubits. *Nature Phys*., 2010, **6**(6), 409–413.
33. Childs, A. M., Chuang, I. L. and Leung, D. W., Realization of quantum process tomography in NMR. *Phys. Rev. A*, 2001, **64**(1), 012314-1 to 7.
34. Chow, J. M. *et al.*, Simple all-microwave entangling gate for fixed-frequency superconducting qubits. *Phys. Rev. Lett*., 2011, **107**(8), 080502-1 to 5.
35. Chow, J. M. *et al.*, Randomized benchmarking and process tomography for gate errors in a solid-state qubit. *Phys. Rev. Lett*., 2009, **102**(9), 090502-1 to 4.
36. De Martini, F., Mazzei, A., Ricci, M. and D'Ariano, G. M., Exploiting quantum parallelism of entanglement for a complete experimental quantum characterization of a single-qubit device. *Phys. Rev. A*, 2003, **67**(6), 062307-1 to 5.
37. Dewes, A. *et al.*, Characterization of a two-transmon processor with individual single-shot qubit readout. *Phys. Rev. Lett.*, 2012, **108**(5), 057002-1 to 5.
38. Hanneke, D., Home, J. P., Jost, J. D., Amini, J. M., Leibfried, D. and Wineland, D. J., Realization of a programmable two-qubit quantum processor. *Nature Phys*., 2010, **6**(1), 13–16.
39. Mitchell, M. W., Ellenor, C. W., Schneider, S. and Steinberg, A. M., Diagnosis, prescription, and prognosis of a Bell-state filter by quantum process tomography. *Phys. Rev. Lett*., 2003, **91**(12), 120402-1 to 4.
40. Neeley, M. *et al.*, Process tomography of quantum memory in a Josephson-phase qubit coupled to a two-level state. *Nature Phys*., 2008, **4**(7), 523–526.
41. O'Brien, J. L., Pryde, G. J., Gilchrist, A., James, D. F. V., Langford, N. K., Ralph, T. C. and White, A. G., Quantum process tomography of a controlled-not gate. *Phys. Rev. Lett*., 2004, **93**(8), 080502-1 to 4.
42. Riebe, M. *et al.*, Process tomography of ion trap quantum gates. *Phys. Rev. Lett.*, 2006, **97**(22), 220407-1 to 4.
43. Weinstein, Y. S., Havel, T. F., Emerson, J., Boulant, N., Saraceno, M., Lloyd, S. and Cory, D. G., Quantum process tomography of the quantum Fourier transform. *J. Chem. Phys*., 2004, **121**(13), 6117–6133.
44. Yamamoto, T. *et al.*, Quantum process tomography of two-qubit controlled-Z and controlled-not gates using superconducting phase qubits. *Phys. Rev. B*, 2010, **82**(18), 184515-1 to 8.
45. Zhang, J., Souza, A. M., Brandao, F. D. and Suter, D., Protected quantum computing: interleaving gate operations with dynamical decoupling sequences. *Phys. Rev. Lett*., 2014, **112**(5), 050502-1 to 5.

46. Shabani, A. *et al.*, Efficient measurement of quantum dynamics via compressive sensing. *Phys. Rev. Lett*., 2011, **106**(10), 100401-1 to 4.
47. Wu, Z., Li, S., Zheng, W., Peng, X. and Feng, M., Experimental demonstration of simplified quantum process tomography. *J. Chem. Phys*., 2013, **138**(2), 024318-1 to 7.
48. D'Ariano, G. M. and Lo Presti, P., Imprinting complete information about a quantum channel on its output state. *Phys. Rev. Lett*., 2003, **91**(4), 047902-1 to 4.
49. Mazzei, A., Ricci, M., De Martini, F. and D'Ariano, G., Pauli tomography: complete characterization of a single qubit device. *Fortschr. Phys*., 2003, **51**(4–5), 342–348.
50. Shukla, A. and Mahesh, T. S., Single-scan quantum process tomography. *Phys. Rev. A*, 2014, **90**(5), 052301-1 to 6.
51. Meiboom, S. and Gill, D., Modified spinecho method for measuring nuclear relaxation times. *Rev. Sci. Instrum*., 1958, **29**(8), 688–691.
52. Uhrig, G. S., Keeping a quantum bit alive by optimized π-pulse sequences. *Phys. Rev. Lett*., 2007, **98**(10), 100504-1 to 4.
53. Viola, L., Knill, E. and Lloyd, S., Dynamical decoupling of open quantum systems. *Phys. Rev. Lett*., 1999, **82**(12), 2417–2421.
54. Viola, L. and Lloyd, S., Dynamical suppression of decoherence in two-state quantum systems. *Phys. Rev. A*, 1998, **58**(4), 2733–2744.
55. Preskill, J., Reliable quantum computers. *Proc. R. Soc. London Ser. A*, 1998, **454**(1969), 385–410.
56. Farhi, E., Goldstone, J., Gutmann, S. and Sipser, M., Quantum computation by adiabatic evolution. arXiv:quant-ph/0001106.
57. Lidar, D. A. and Whaley, K. B., Decoherence-free subspaces and subsystems. In *Irreversible Quantum Dynamics*, Springer, 2003, pp. 83–120.
58. Hegde, S. S. and Mahesh, T. S., Engineered decoherence: characterization and suppression. *Phys. Rev. A*, 2014, **89**(6), 062317-1 to 5.
59. Cory, D. G., Price, M. D. and Havel, T. F., *Physica D*, 1998, **120**(1–2), 82–101.
60. Biercuk, M. J., Doherty, A. C. and Uys, H., Dynamical decoupling sequence construction as a filter-design problem. *J. Phys. B*., 2011, **44**(15), 154002-1 to 15.
61. Biercuk, M. J., Uys, H., VanDevender, A. P., Shiga, N., Itano, W. M. and Bollinger, J. J., Optimized dynamical decoupling in a model quantum memory. *Nature*, 2009, **458**(7241), 996–1000.
62. Pan, Y., Xi, Z.-R. and Gong, J., Optimized dynamical decoupling sequences in protecting two-qubit states. *J. Phys. B*, 2011, **44**(17), 175501-1 to 8.
63. Yuge, T., Sasaki, S. and Hirayama, Y., Measurement of the noise spectrum using a multiple-pulse sequence. *Phys. Rev. Lett.*, 2011, **107**(17), 170504-1 to 4.
64. Moussa, O., Ryan, C. A., Cory, D. G. and Laamme, R., Testing contextuality on quantum ensembles with one clean qubit. *Phys. Rev. Lett*., 2010, **104**(16), 160501-1 to 4.

ACKNOWLEDGEMENTS. We thank Prof. Anil Kumar (IISc, Bengaluru), Prof. Usha Devi (Bangalore University), Prof. A. K. Rajagopal (Inspire Institute, USA), and Dr Anirban Hazra (IISER, Pune), for discussions. Projects described in this article were partly supported by the DST Project No. SR/S2/LOP-0017/2009.

doi: 10.18520/v109/i11/1987-1996